Fusion hindrance and roles of shell effects in superheavy mass region

Y. Aritomo

Flerov Laboratory of Nuclear Reactions, JINR, Dubna, Russia

Abstract

We present the first attempt of systematically investigating the effects of shell correction energy for a dynamical process, which includes fusion, fusion-fission and quasi-fission processes. In the superheavy mass region, for the fusion process, shell correction energy plays a very important role and enhances the fusion probability when the colliding partner has a strong shell structure. By analyzing the trajectory in three-dimensional coordinate space with the Langevin equation, we reveal the mechanism of the enhancement of the fusion probability caused by 'cold fusion valleys'. The temperature dependence of shell correction energy is considered.

Key words: superheavy elements, fluctuation-dissipation dynamics, fusion-fission process, quasi-fission process

1 Introduction

In a heavy-ion fusion reaction, with increasing atomic numbers of the target and projectile, it becomes more difficult to produce a compound nucleus owing to the strong Coulomb repulsion and strong dissipation forces. In the superheavy mass region, this difficulty is more pronounced. Although the mechanism of the fusion-fission reaction in the heavy-mass region is not clear, generally we recognize the existence of fusion hindrance (1; 2; 3).

The dynamical aspects of the fusion-fission mechanism have been investigated as a time evolution of the nuclear shape with friction. In the 1980s, a mean trajectory calculation in the nuclear deformation space using a stochastic equation, known as the extra-push model, was performed by Swiatecki and coworkers (4; 5). In the superheavy-mass region, however, even if substantial extra push energy is supplied, it is very difficult for the mean trajectory to reach the spherical region owing to a strong dissipation. It is necessary to apply fluctuation-dissipation dynamics (6).

The simplified calculation that included the one-dimensional diffusion model was applied to cold fusion reactions (7). With one adjustable parameter, the results showed a good agreement with many experimental data, not only maximum cross sections, but also the optimum energies and widths of the excitations functions. In the present study, we concentrate to discuss the fusion process using the more realistic model.

Fusion hindrance is mainly caused by the macroscopic properties of the colliding partner (8). On the contrary, fusion is enhanced by the deformation and shell structure of the nuclei, which we call fusion enhancement (9; 10; 11; 12). In experiments, especially in the case of a cold fusion reaction, these advantages are used to synthesize superheavy nuclei (13; 14). To understand the fusion mechanism clearly, it is better to treat separately fusion hindrance and fusion enhancement, that is to say, the macroscopic and microscopic aspects, respectively.

In our previous study (8), we focused, in particular, on fusion hindrance, in the superheavy mass region. We have presented the origin of the fusion hindrance systematically by conducting a trajectory calculation in three-dimensional coordinate space. To see the fundamental mechanism of the fusion hindrance, we employed the potential energy of the liquid drop model, and analyzed the mean trajectory. From the behavior of the trajectory, we can understand the mechanism that the fusion probability decreases exponentially as the Z number of the fused system increases. It is concluded that the fusion hindrance in a system with Z greater than 102 is explained by considering the fragment deformation to be an important factor.

Considering aspects of the fusion enhancement, we focus on the influence of the shell effect. The nuclear structure of the projectile-target combinations is related to the touching probability, but it also influences the dynamics from the touching point to the compound nucleus in the superheavy mass region (11; 12). In our approach (6; 15; 8), as parameters related to the microscopic effects, in principle we can introduce the shell correction energy on the potential energy surface and the transport coefficients calculated using the microscopic model (16; 17; 18). In the former case, we can see 'cold fusion valleys' in the potential energy surface, which have been suggested in references (19; 20). It is said that these valleys lead to the enhancement of the fusion probability. Here, we investigate precisely how the trajectory is affected by shell correction energy, and how the fusion probability is changed.

In fact, shell correction energy depends on the nuclear temperature. In a dynamical process, the nuclear temperature changes owing to the dissipation of the kinetic energy of the relative motion. Therefore, we must discuss the fusion process taking into account the time evolution of the potential energy surface, which is controlled by nuclear friction, since the dissipation depends

on the nuclear friction. We clarify the effect of the temperature-dependent shell correction energy in the fusion process.

For clarity, in this paper, we consider the 'dynamical process' as the whole process from the contact point to the spherical nucleus or re-separated one. It includes the fusion, quasi-fission and deep quasi-fission processes, which are defined in reference (6).

In section 2, we briefly explain our framework for the study and the model. We precisely investigate the effects of cold fusion valleys in section 3. In this section, using the potential energy surface of the full shell correction energy, we discuss the mechanism of the enhancement of the fusion probability by cold fusion valleys. In section 4, taking into account the temperature dependence of shell correction energy, we discuss the fusion process. In section 5, we present a summary and further discussion to clarify the reaction mechanism in the superheavy mass region.

2   Model

Using the same procedure as described in reference (6) to investigate the dynamical process, we use the fluctuation-dissipation model and employ the Langevin equation. We adopt the three-dimensional nuclear deformation space given by two-center parameterization (21; 22). The three collective parameters involved in the Langevin equation are as follows: z_0 (distance between two potential centers), δ (deformation of fragments) and α (mass asymmetry of the colliding nuclei); $\alpha = (A_1 - A_2)/(A_1 + A_2)$, where A_1 and A_2 denote the mass numbers of the target and the projectile, respectively.

The parameter δ is defined as $\delta = 3(a - b)/(2a + b)$, where a and b denote the half length of the axes of ellipse in the z and ρ directions, respectively as expressed in Fig. 1 in reference (21). We assume that each fragment has the same deformations as the first approximation. δ is related to the deformation parameter β_2, which is familiar with us, as

$$\beta_2 = \frac{\delta}{\sqrt{\frac{5}{16\pi}}(3 - \delta)}. \tag{1}$$

The neck parameter ϵ is the ratio of the smoothed potential height to the original one where two harmonic oscillator potentials cross each other. It is defined in the same manner as reference (21). With $\epsilon < 1$, the surface of two fragments shows the smooth curve at the connecting point of them. On the other hand, in the case of $\epsilon = 1$, the two fragments are connected with a sharp

point like a top of cone. In the present calculation, ϵ is fixed to be 1.0, so as to retain the contact-like configuration more realistically for two-nucleus collision.

The multidimensional Langevin equation is given as

$$\frac{dq_i}{dt} = \left(m^{-1}\right)_{ij} p_j,$$
$$\frac{dp_i}{dt} = -\frac{\partial V}{\partial q_i} - \frac{1}{2} \frac{\partial}{\partial q_i} \left(m^{-1}\right)_{jk} p_j p_k - \gamma_{ij} \left(m^{-1}\right)_{jk} p_k + g_{ij} R_j(t),$$

$$(2)$$

where a summation over repeated indices is assumed. q_i denotes the deformation coordinate specified by z_0, δ and α. p_i is the conjugate momentum of q_i. V is the potential energy, and m_{ij} and γ_{ij} are the shape-dependent collective inertia parameter and dissipation tensor, respectively. A hydrodynamical inertia tensor is adopted in the Werner-Wheeler approximation for the velocity field, and the wall-and-window one-body dissipation is adopted for the dissipation tensor (23; 24; 25). The normalized random force $R_i(t)$ is assumed to be white noise, i.e., $\langle R_i(t) \rangle = 0$ and $\langle R_i(t_1) R_j(t_2) \rangle = 2\delta_{ij}\delta(t_1 - t_2)$. The strength of random force g_{ij} is given by $\gamma_{ij}T = \sum_k g_{ij}g_{jk}$, where T is the temperature of the compound nucleus calculated from the intrinsic energy of the composite system. The potential energy is defined as

$$V(q, l, T) = V_{LD}(q) + \frac{\hbar^2 l(l+1)}{2I(q)} + V_{SH}(q, T), \qquad (3)$$

$$V_{LD}(q) = E_S(q) + E_C(q), \qquad (4)$$

$$V_{SH}(q, T) = E_{shell}^0(q)\Phi(T), \qquad (5)$$

where $I(q)$ is the moment of inertia of a rigid body at deformation q. V_{LD} and V_{SH} are the potential energy of the finite-range liquid drop model and the shell correction energy taking into account the temperature dependence. E_{shell}^0 is the shell correction energy at $T = 0$. The temperature dependent factor $\Phi(T)$ is discussed in the section 4.1. E_S and E_C denote a generalized surface energy (26) and Coulomb energy, respectively. The centrifugal energy arising from the angular momentum l of the rigid body is also considered. The detail is explained in reference (6). The intrinsic energy of the composite system E_{int} is calculated for each trajectory as

$$E_{int} = E^* - \frac{1}{2} \left(m^{-1}\right)_{ij} p_i p_j - V(q, l, T), \qquad (6)$$

where E^* denotes the excitation energy of the compound nucleus. E^* is given

by $E^* = E_{cm} - Q$, where Q and E_{cm} denote the $Q-$value of the reaction and the incident energy in the center-of-mass frame, respectively. At $t = 0$, each trajectory starts from the contact point which is defined as $R_{touch} = R_p + R_t$, where R_p and R_t are the radii of projectile and target, respectively.

As discussed in reference (6), we assumed that the kinetic energy of the relative motion does not dissipate during the approaching process. However, to investigate the effect of the energy dissipation during the approaching process, we introduce a parameter E_{diss} which is the intrinsic energy converted from the relative kinetic energy before both nuclei touch. The discussion on this issue is given in section 4.3. At the contact point, the initial velocity is directed only in the $-z$ direction, and the components of the initial velocities along the δ and α directions are both assumed to be zero (6; 27).

3 Effects of shell correction energy in fusion process

In our previous study (8), we focused on the fusion hindrance from the macroscopic point of view. We employed the potential energy of the liquid drop model and analyzed the mean trajectory excluding the final term on the right-hand side of Eq. (2) and used $\Phi(T) = 0$ in Eq. (5). We presented the origin of the fusion hindrance systematically.

Here, we investigate the fusion enhancement from the microscopic point of view. The nuclear structure of the projectile-target combinations is related to the touching probability, but it also influences the dynamics from the contact point to the compound nucleus (11; 12). We focus on the dynamics taking into account the shell effect after both nuclei touch. Within our model (6; 15; 8), we introduce the potential energy surface with the shell correction energy.

Figure 1 shows the potential energy surface of the liquid drop model (a) and with shell correction energy (b) for $^{292}114$ in the $z - \alpha$ space $(\delta = 0)$, which is calculated using the two-center shell model code (28; 29). When we consider the shell correction energy on the potential energy surface, we can see pronounced valleys, that lead to the compound nucleus. The valleys are called 'cold fusion valleys' (19; 20). It is said that these valleys enhance the fusion probability.

We can see such shell structure in another calculation (30). Single particle level diagrams in reaction $^{70}Zn+^{208}Pb$ were calculated by a macroscopic-microscopic model. It shows that the entrance-channel fragment-shell effects remain far inside the touching point.

In this section, we discuss the effect of shell correction energy on the dynamical
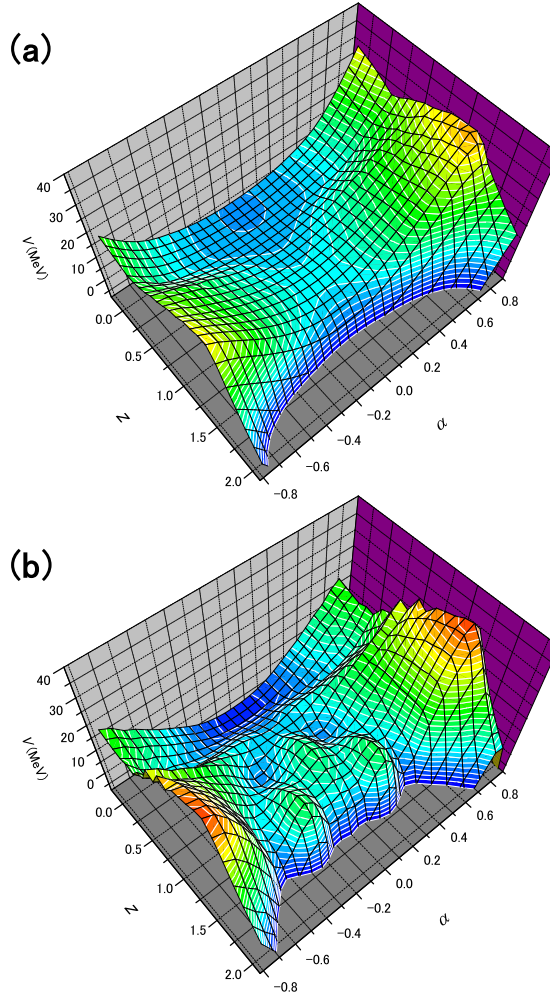
Fig. 1. Potential energy of the liquid drop model (a) and with shell correction energy (b) for $^{292}114$ in the $z - \alpha$ space ($\delta = 0$). The calculation is done using the two-center shell model code (28; 29).

process using trajectory calculation.

3.1 Effect of cold fusion valleys on fusion process

As our first attempt, we employ the potential energy of the liquid drop with the full shell correction energy, which corresponds to the potential energy surface at $T = 0$ MeV. This potential energy is represented by $V_{LD} + V_{SH}(q, T = 0)$, or $V_{LD} + E^0_{shell}$ by Eq. (5). We mainly discuss head-on collision, that is to say, the process for $l = 0$, because the general mechanism of the trajectory's behavior does not change essentially in any of the angular momentum cases, although the potential landscape changes with angular momentum.
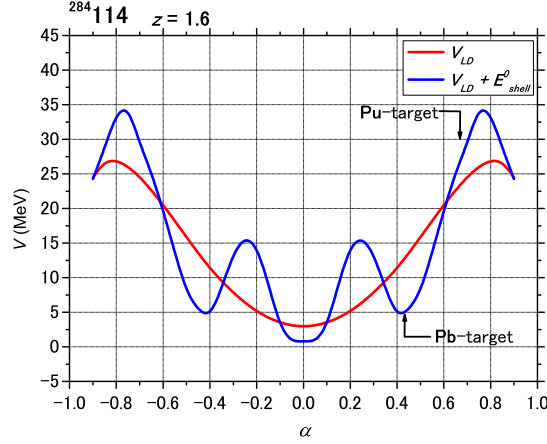
Fig. 2. Potential energy of V_{LD} and $V_{LD} + E^0_{shell}$ for $^{284}114$ at $z = 1.6$, which are denoted by the red and blue lines, respectively. The calculation is done using the two-center shell model code. The combination of the Pb-target and Pu-target are indicated.

Figure 2 shows the potential energies V_{LD} and $V_{LD}+E^0_{shell}$ for $^{284}114$ at $z = 1.6$, which the potential energies correspond to a location near the contact point. The red and blue lines denote V_{LD} and $V_{LD} + E^0_{shell}$, respectively. The shell correction energy in the reaction system where the target corresponds to Pb is significant, and is indicated in Fig. 2. Actually, a Pb target is chosen in a cold fusion reaction, in order to suppress the excitation energy of a compound nucleus (31).

To investigate the effects of the cold fusion valleys, we compare the fusion probabilities at different injection points, where the shell correction energy has very large negative and positive values, such as $\alpha = 0.46$ and 0.24 in Fig. 2, respectively.

The former corresponds to the reaction ^{76}Ge + ^{208}Pb, which is a cold fusion reaction, and the latter corresponds to ^{108}Ru + ^{176}Yb. Figure 3(a) shows sample trajectories that are projected onto the $z - \alpha$ ($\delta = 0$) plane of the potential energy surface for $^{284}114$. The contact point is marked by (+). The light yellow line denotes the trajectory with the starting point $\alpha_0 = 0.46$ at the incident energy corresponding to the excitation energy of the compound nucleus $E^*=20$ MeV. This trajectory appears to move along the valley till $z \sim 1.0$. Then it approaches the $z \sim 0$ region.

On the other hand, the trajectory with the starting point $\alpha_0 = 0.24$ moves till $z \sim 1.0$ without changing the mass asymmetry parameter α, which is denoted by the white line. It seems that the trajectory overcomes the mountain located at $z = 1.4$ and $\alpha = 0.24$. This trajectory does not move along the bottom of the valley. We can say that this trajectory is not influenced by the valley till
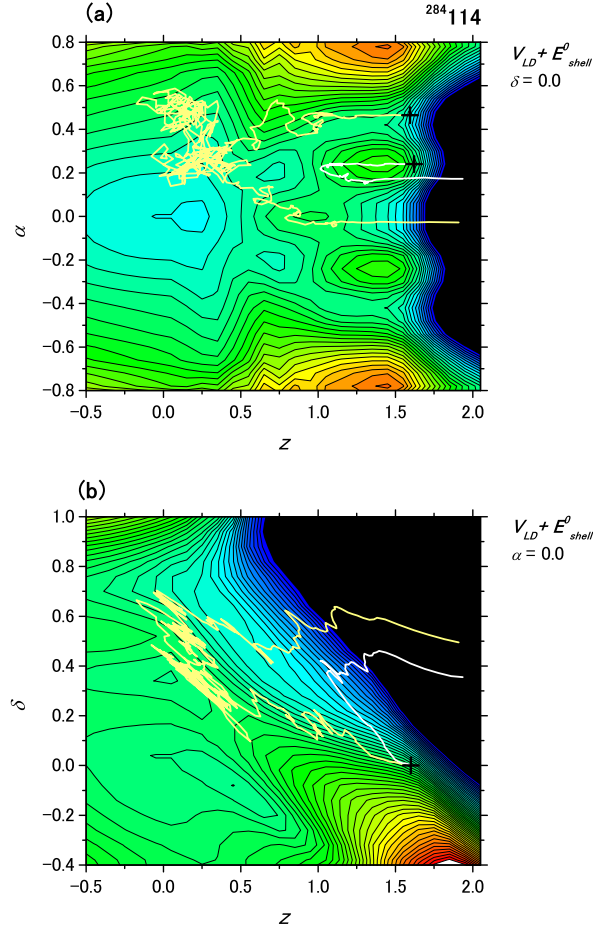
Fig. 3. Sample trajectories projected onto the $z - \alpha$ plane at $\delta = 0.0$ (a) and the $z - \delta$ plane at $\alpha = 0.0$ (b) of $V_{LD} + E^0_{shell}$ for $^{284}114$. The light yellow and white lines denote the trajectories which start at $\alpha = 0.46$ and 0.24 at $E^* = 20$ MeV. Symbols are given in the text.

$z \sim 1.0$. Then it turns in the $+z$ direction, which corresponds to the fission region.

We project the trajectories of Fig. 3(a) onto the $z - \delta$ plane at $\alpha = 0$, as shown in Fig. 3(b). The trajectory with $\alpha_0 = 0.46$ can approach the compact shape region, but it is not trapped by the pocket at the ground state. The trajectory with $\alpha_0 = 0.24$ moves rapidly in the $+\delta$ direction and enters the fission region. We can say that the former is a deep quasi-fission process (DQF) and the latter is a quasi-fission process (QF) (6; 8).

To understand why these two trajectories take different paths, we precisely analyze the trajectory's behavior with the potential energy surface near the contact point. The potential landscape near the contact point is very impor-
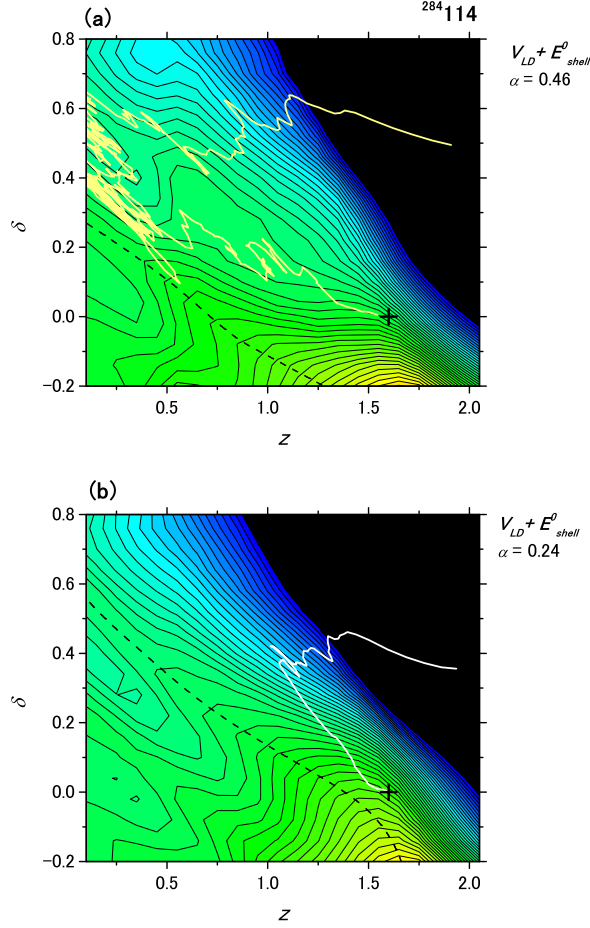
Fig. 4. The trajectories in Fig. 3(b) are projected on to the $z - \delta$ plane near the contact point. (a) $\alpha = 0.46$ and (b) $\alpha = 0.24$. The dashed line denotes the ridge line of the potential energy surface.

tant for deciding the destiny of the trajectory (15). Figure 4(a) shows the trajectory with $\alpha_0 = 0.46$, which is projected onto the $z - \delta$ plane ($\alpha = 0.46$). The trajectory is the same as that in Fig. 3. The dashed line denotes the ridge line. The contact point is far from the ridge line, but it does not mean the trajectory moves into the fission region immediately. On the potential energy surface near the contact point, although we can see the steep slope in the $+\delta$ direction, there are no significant barriers in the $-z$ direction from the contact point. Therefore, first the trajectory moves in the $-z$ direction while maintaining $\delta \sim 0$. Owning to the shell correction energy, a flat potential region exists around $z \sim 0.8$ and $\delta \sim 0.25$. This flat region prevents the trajectory from moving in the $+\delta$ direction rapidly. Finally, the trajectory can enter the region near $z \sim 0$.

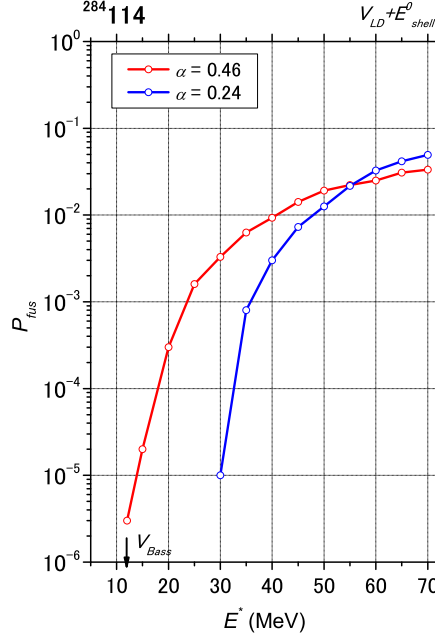Figure 4(b) shows the trajectory with $\alpha_0 = 0.24$, which is projected onto the

Fig. 5. Fusion probabilities for the initial values $\alpha_0 = 0.46$ and $\alpha_0 = 0.24$, which are denoted by the red and blue lines, respectively.

$z - \delta$ plane ($\alpha = 0.24$). The contact point is located near the ridge line, but a substantial barrier exists in the $-z$ direction from the contact point. To avoid the barrier, the trajectory moves in the $+\delta$ direction rapidly.

Figure 5 shows the fusion probabilities for $\alpha_0 = 0.46$ and $\alpha_0 = 0.24$, which are denoted by the red and blue lines, respectively. The potential energy at the contact point for $\alpha = 0.46$ is lower than that for $\alpha = 0.24$, as shown in Fig. 2. Therefore, at low excitation energy, the former fusion probability is larger than the latter one because in the former case the available kinetic energy at the contact point is larger than that in the latter case. The arrow indicates the Coulomb barrier (32). At high excitation energy, the fusion probabilities of these two cases are not markedly different because the kinetic energy at the contact point is rather large in both cases.

3.2 Evolution of cold fusion valleys on dynamical process

Usually, cold fusion valleys are discussed using the potential energy surface on the $z - \alpha$ plane with $\delta = 0$, as in Fig. 1(b). However, in the dynamical process, the trajectory moves in the large $+\delta$ direction. Therefore, we should discuss the cold fusion valleys with the dynamical evolution of the δ parameter. For the $\delta = 0$ case, we can see that the cold fusion valleys are remarkable. With changing δ in the dynamical process, the cold fusion valleys also change. While
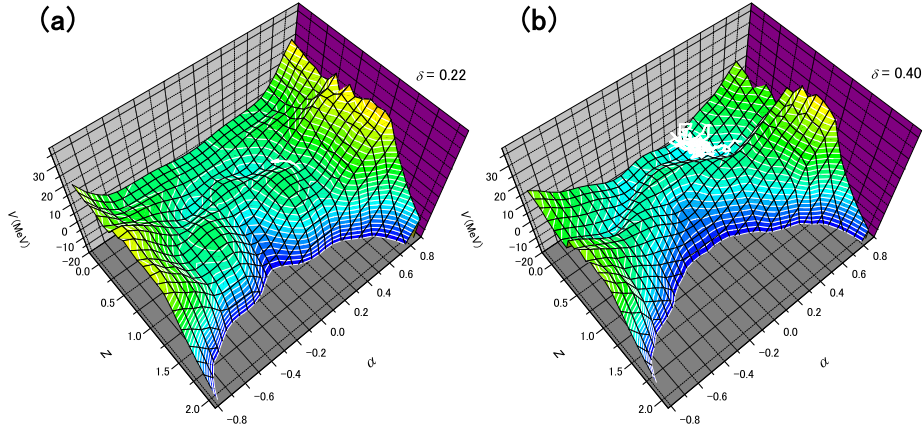
10

Fig. 6. Potential energy surface $V_{LD} + E^0_{shell}$ in the $z - \alpha$ space at (a) $\delta = 0.2$ and (b) $\delta = 0.4$ for $^{284}114$ with a trajectory.

the trajectory moves from $z \sim 1.25$ to 0.5, δ changes to 0.2. Figure 6(a) shows the potential energy surface on the $z - \alpha$ plane at $\delta = 0.2$ with the trajectory. The position and depth of the cold fusion valleys slightly change. After moving along the valley, the trajectory enters the region $z < 0.5$. In this region, δ is more than 0.4. Figure 6(b) shows the potential energy at $\delta = 0.4$ with the trajectory. We can see that the cold fusion valleys have already disappeared.

3.3 Roles of shell effects on fusion process

Owing to the shell correction energy, we discuss another important effect to enhance the fusion probability. In the discussion on fusion hindrance (8), we indicated that the turning point is very important. Figure 7(a) shows the potential energy surface of V_{LD} for $Z=102$ at the turning point on the $z - \delta$ plane, that is to say, α corresponds to the value at the turning point. The mean trajectory is denoted by the white line. The red line denotes the trajectory taking into account the fluctuation. At the turning point ($z \sim 0.3, \delta \sim 0.5$), the trajectory moves in the fission direction owing to the potential landscape (8).

However, when we take into account the shell correction energy shown in Fig. 7(c), a temporary pocket appears at the turning point (indicated by A), which we call the second pocket (15). Figure 7(d) shows the potential energy at $\alpha = 0$. The pocket (indicated by B) corresponds to the ground state. The trajectory is trapped in the second pocket A at the turning point, and is blocked from going to the fission area (15). While the trajectory remains in pocket A, the mass asymmetry is relaxed, and the large pocket B appears at $\alpha \sim 0$. Then, the trajectory moves to pocket B. Pocket A helps the trajectory
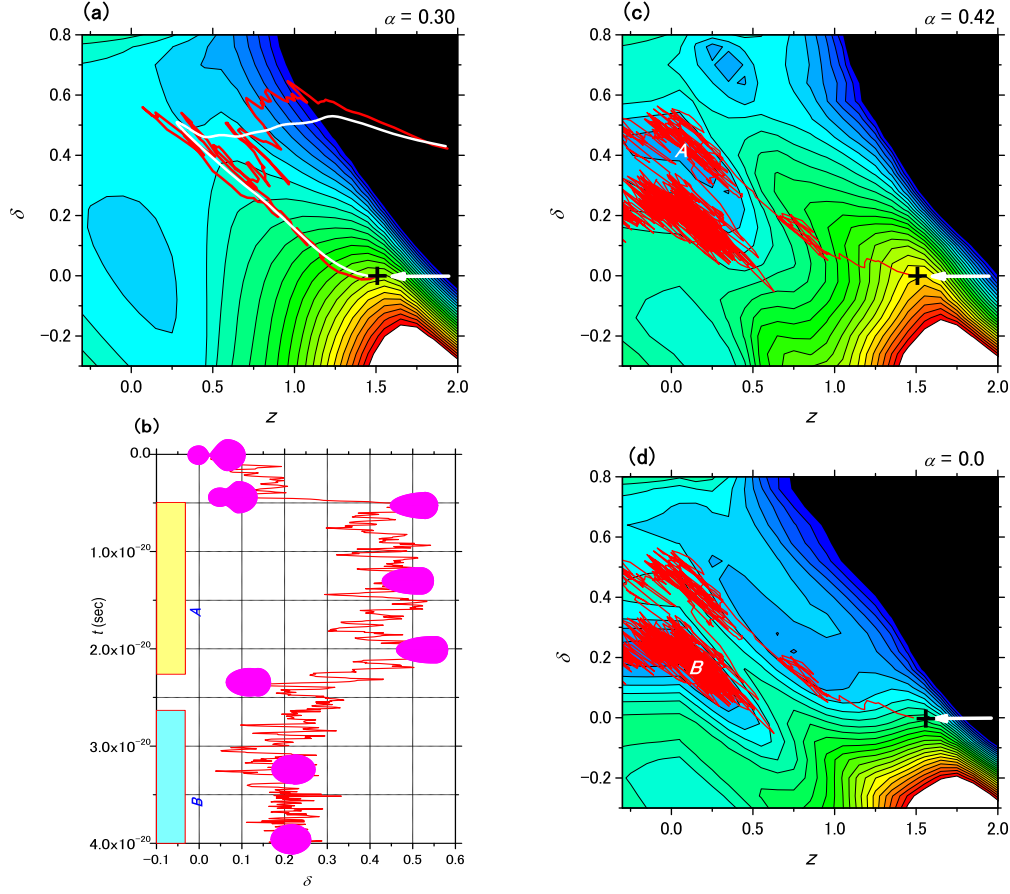
11

Fig. 7. Sample trajectories projected onto the $z - \delta$ plane at α which corresponds to the turning point. (a) V_{LD} case and (c) $V_{LD} + E^0_{shell}$ case for ^{256}No. $V_{LD} + E^0_{shell}$ with $\alpha = 0.0$ is shown in (d). The evolution of nuclear shape is presented in (b).

enter the region corresponding to the compound nucleus.

Figure 7(b) shows the time evolution of nuclear shape. The horizontal axis denotes δ. After the contact point, the trajectory moves in the large δ direction rapidly, then it is trapped in the second pocket A. At this moment, the neck of nuclear shape is rather large owing to the large δ, so that the mass asymmetry is relaxed easily while the trajectory remains in pocket A. As α approaches zero, the trajectory moves into pocket B. It corresponds to the compound nucleus.
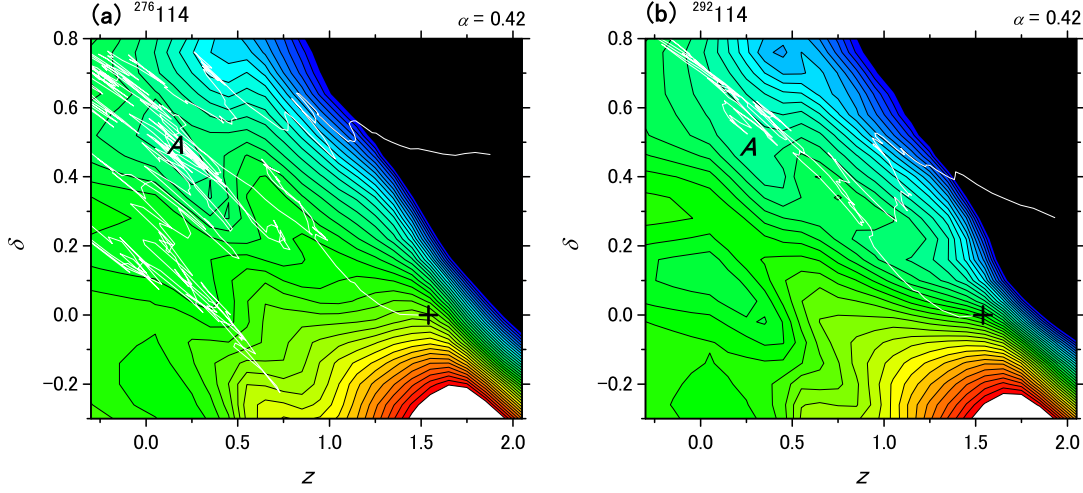
Fig. 8. Sample trajectory projected onto the $z - \delta$ plane at $\alpha = 0.42$ of $V_{LD} + E^0_{shell}$ for (a) $^{276}114$ (deformed nucleus) and (b) $^{292}114$ (spherical one). The trajectory starts at $\alpha = 0.67$ and $E^* = 40$ MeV. Symbols are given in the text.

3.4 Difference between spherical and deformed compound nuclei

In the previous section, we pointed out the role of the second pocket in the fusion process. However, the second pocket does not always enhance the fusion probability. As regards the position of the second pocket, we discuss the difficulty of synthesizing superheavy elements.

In general, the position at the ground state of the compound nucleus is decided by the shell correction energy. As discussed above, in the reaction ^{48}Ca$+$ ^{208}Pb, the ground state of the compound nucleus ^{256}No is located at $\delta \sim 0.2$, which is deformed. Therefore, the second pocket A is located at a δ with a more deformed shape ($\delta \sim 0.4$), as shown in Fig. 7(c), which simply corresponds to the turning point. In this case, pocket A assists the trajectory in entering the region corresponding to the compound nucleus.

However, in the superheavy mass region ($Z > 110$), the nuclear shape at the ground state is spherical, which has a large shell correction energy. For example, in the reaction ^{48}Ca$+$ ^{244}Pu ($\alpha = 0.67$), the ground state of the compound nucleus $^{292}114$ is located at $\delta = 0$. In this case, the second pocket is located at $\delta \sim 0.2$, which does not correspond to the turning point ($\delta \sim 0.4$). Therefore, many trajectories return in the $+z$ direction. This is one of the difficulties in making spherical compound nuclei such as $^{292}114$.

13

To show the role of the second pocket, we compare the trajectories forming the compound nuclei $^{276}114$ (deformed) and $^{292}114$ (spherical). Figures 8(a) and (b) show sample trajectories, which are projected onto the $z - \delta$ plane at $\alpha = 0.42$ of $V_{LD} + E^0_{shell}$, for $^{276}114$ and $^{292}114$, respectively. Both trajectories start at $\alpha = 0.67$ with the incident energy corresponding to the excitation energy of the compound nucleus, E^*=40 MeV. In this case, $\alpha \sim 0.42$ corresponds to the turning point.

In Fig. 8(a), a small pocket exists at $z \sim 0.25$ and $\delta \sim 0.5$, which is the second pocket (indicated by A). The trajectory is trapped by pocket A and is prevented from moving into the reseparation region. Then, it moves to the main pocket, which is located at around $z \sim 0, \delta \sim 0.2$ and $\alpha \sim 0$. The shell correction energy at the ground state is about 5.0 MeV; therefore, the trajectory easily escapes from the main pocket. In Fig. 8(b), which corresponds to the reaction ^{48}Ca+^{244}Pu, the second pocket does not exist at around $z \sim 0.25$ and $\delta \sim 0.5$ because the compound nucleus $^{292}114$ is spherical. We can see that it is difficult for the trajectory to enter the spherical region. The trajectory returns to the fission region.

Figure 9 shows the fusion probabilities for forming the compound nuclei $^{292}114$ and $^{276}114$, which are denoted by the blue and red lines, respectively. We use the initial value of $\alpha = 0.67$ for both cases. The fusion probability of $^{276}114$ is larger than that of $^{292}114$, owing to the second pocket, which is located at the deformed shape.

4 Effect of temperature-dependent shell correction energy

In the previous section, we used the full shell correction energy for the potential energy surface. However, the shell correction energy actually depends on the nuclear temperature T. For the dynamical calculation for the fusion process, the temperature dependence of shell correction energy has not been considered sufficiently in many publications.

In this section, we discuss the temperature dependence of the shell correction energy and how the fusion process is affected. Considerable effort has been made to investigate the temperature dependence of the level density parameter (33; 34) and applied to the calculation of the statistical model for the fission process (35). The temperature dependence of the potential energy surface has been investigated in references (36; 37). Here, we discuss the effect of this dependence on the fusion process on the basis of dynamical calculations.
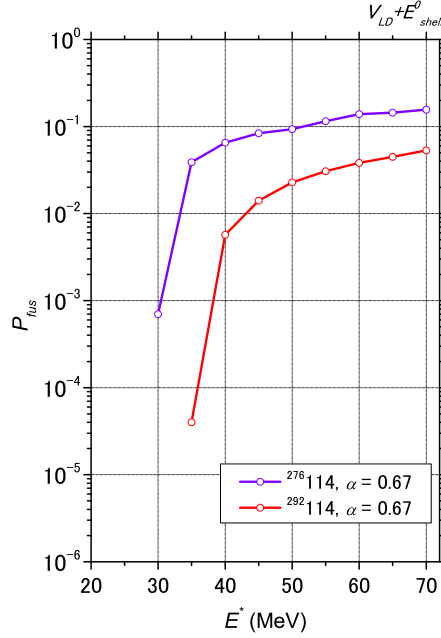
Fig. 9. Fusion probabilities for forming the compound nuclei $^{292}114$ (spherical) and $^{276}114$ (deformed), which are denoted by the blue and red lines, respectively. We use the initial value of $\alpha = 0.67$ for both cases.

4.1 Temperature dependence of shell correction energy

The temperature dependence of shell correction energy can be extracted from the free energy calculated using single particle energies, which is obtained from the two-center shell model code (28; 29). The procedure is given precisely in reference (38). The temperature dependence of shell correction energy calculated by this method is represented by $E_{shell}(q, T)$.

The ratio of shell correction energies, $E_{shell}(q, T)/E_{shell}(q, T = 0)$, in the spherical region for $^{292}114$ is shown in Fig. 10(a) by the solid line. As discussed in reference (38), our result is consistent with the parameterization of the factor $\Phi(T)$,

$$\Phi(T) = \exp\left(-\frac{aT^2}{E_d}\right), \tag{7}$$

following the work by Ignatyuk *et al.* (33), where a denotes the level density parameter of the constant value $a = A/8$. The shell damping energy E_d is chosen as 20 MeV, which is given by Ignatyuk *et al.* (33). This parameterization is denoted by the open circles in Fig. 10(a), which shows a tendency similar to that of the solid line.
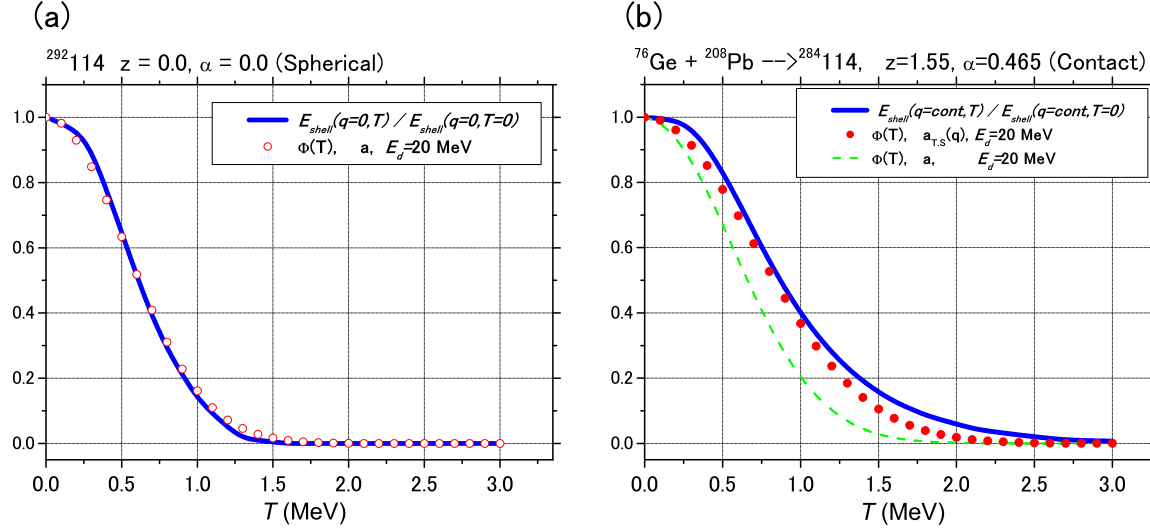
15

Fig. 10. Calculated temperature dependence of shell correction energy. (a) For $^{292}114$ at $q = 0$ (the spherical shape), compared with Ignatyuk's parameterization with $a = A/8$ and $E_d = 20$ MeV. (b) For ^{76}Ge$+^{208}$Pb reaction at the contact point. The symbols and lines are explained in the text.

In the fusion process, it is important to determine $E_{shell}(q, T)$ near the contact point of the colliding partner. The potential landscape near the contact point mainly decides the destiny of the trajectory in the dynamical process. Using the same procedure, we calculate the temperature dependence of shell correction energy at the contact point $E_{shell}(q = cont, T)$ for the reaction ^{76}Ge$+^{208}$Pb. In Fig. 10(b), the blue line denotes $E_{shell}(q = cont, T)/E_{shell}(q = cont, T = 0)$. This tendency is different from that of the spherical shape case, which is denoted by the dashed line. In Eq. (7), when we take into account the nuclear deformation dependence of the level density parameter $a_{T.S.}(q)$ (39), our result can be fitted using $E_d = 20$ MeV, denoted by the open circles. The result shows the similar tendency of the blue line.

4.2 Trajectory behavior on temperature-dependent potential energy surface

In the fission process, the time evolution of the potential energy surface affects the dynamical process considerably. Owing to the neutron emission from the compound nucleus, the temperature of the nucleus decreases, and the shell correction energy recovers. The time scale of the variation of the potential energy surface affects the dynamics of the fission process (38).
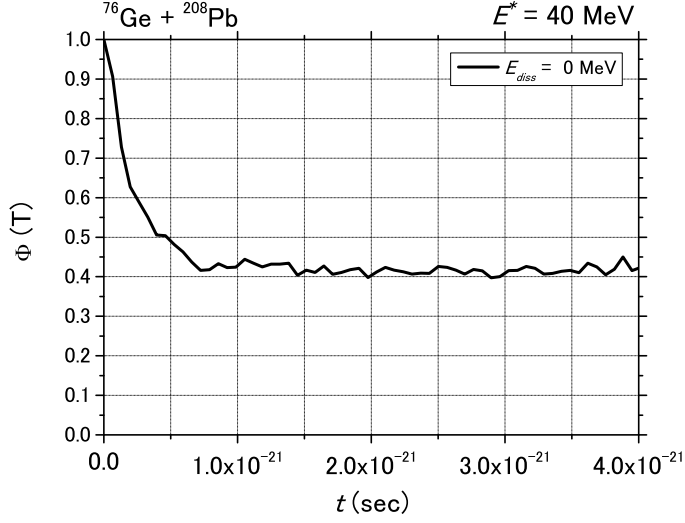
Fig. 11. Time evolution of $\Phi(T)$ for a trajectory in the reaction ^{76}Ge+^{208}Pb at $E^* = 40$MeV with $E_{diss} = 0$ MeV.

Here, we focus on the effect of the temperature-dependent shell correction energy on the fusion process. In the dynamical calculation, we analyze the trajectory on the temperature-dependent potential energy surface, which is concerned with the intrinsic energy E_{int} of the system.

Within our model, the time evolution of E_{int} is controlled by the friction tensor γ. Also, E_{int} is connected with E_{diss} at the contact point (27). Here, we clarify the relationship among these variables and the mechanism of the fusion process.

We start the dynamical calculation from the contact point using the Langevin equation. E_{diss} is treated as a parameter of the initial condition. Discussions on this issue have been given in references (40; 27). In fact, E_{diss} is related to the dynamics in the approaching process. Considering E_{diss} as a parameter, we investigate the effect of E_{diss} on the trajectory in the process after the both nuclei touch. Then, in the next section, we discuss the effect of the friction tensor γ.

Before we discuss the effect of the different E_{diss}'s on the dynamical process, we analyze the trajectory under the influence of the temperature-dependent shell correction energy, using the same initial condition as $E_{diss} = 0$ MeV in the previous calculation. We employ the potential energy surface $V_{LD}+V_{SH}(T = 0)$ and $V_{LD} + V_{SH}(T)$ in the reaction ^{76}Ge+^{208}Pb.

When we use $V_{LD} + V_{SH}(T)$ as the potential energy surface, as the intrinsic energy that is transformed from kinetic energy increases, some part of the shell
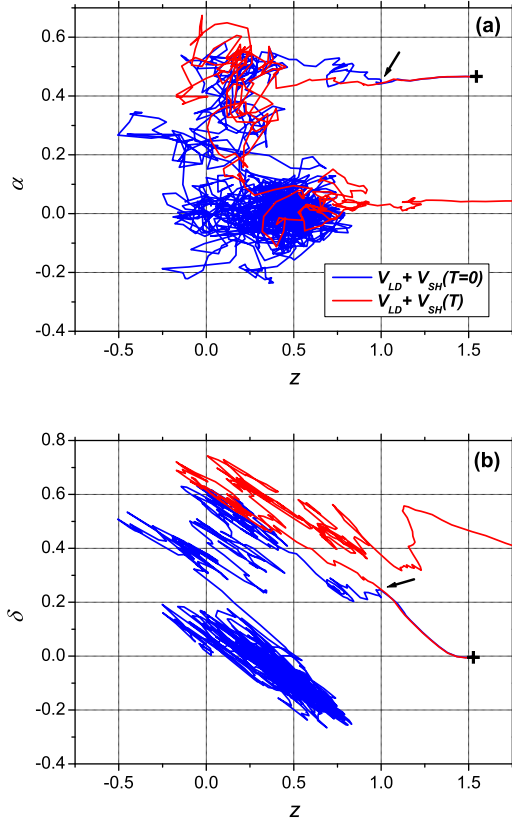
Fig. 12. Sample trajectory on $V_{LD} + V_{SH}(T = 0)$ and $V_{LD} + V_{SH}(T)$ in the reaction ^{76}Ge+^{208}Pb at $E^* = 40$ MeV, which are denoted by blue and red lines, respectively. The trajectories are projected onto (a) the $z - \alpha$ plane and (b) the $z - \delta$ plane, respectively. Symbols are given in the text.

correction energy disappears. Figure 11 shows the time evolution of $\Phi(T)$ for a trajectory at $E^* = 40$ MeV. At the contact point, where $t = 0$ in the calculation, owing to the assumption $E_{diss} = 0$ MeV, which corresponds to $E_{int} = 0$ MeV, the full shell correction energy is indicated. Then, till $t \sim 1.0 \times 10^{-21}$ sec, more than 50% of the shell correction energy disappears owing to the strong friction tensor. During this extremely short reaction time, the kinetic energy dissipates into the intrinsic energy, which has been discussed in reference (15).

As consequence, such variation of the potential energy surface gives the influence on the trajectory's behavior. Figure 12 shows sample trajectories on $V_{LD} + V_{SH}(T = 0)$ and $V_{LD} + V_{SH}(T)$, which are denoted by the blue and red lines. The trajectories are projected onto the $z - \alpha$ plane and $z - \delta$ plane, which are shown in (a) and (b), respectively. The (+) denotes the point of contact in the system. Both trajectories in Fig. 12 are calculated using the
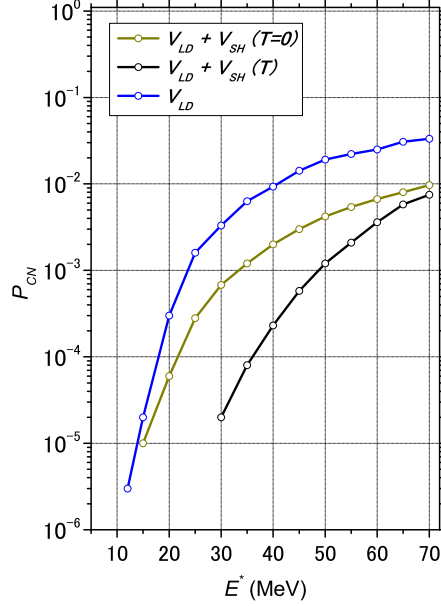
Fig. 13. Fusion probabilities P_{CN} in the reaction ^{76}Ge+^{208}Pb for each potential energy with $E_{diss} = 0$ MeV. The blue and red lines denote P_{CN} with $V_{LD}+V_{SH}(T = 0)$ and $V_{LD} + V_{SH}(T)$, respectively. P_{CN} with V_{LD} is represented by the black line.

same random numbers. After $t = 7.9 \times 10^{-22}$ sec, which is indicated by the black arrow, trajectories separate along different paths owing to the different potential energy surfaces. The trajectory with $V_{LD} + V_{SH}(T = 0)$ takes the fusion process. On the other hand, the trajectory with $V_{LD} + V_{SH}(T)$ takes the deep quasi-fission process. This is brought about by the disappearance of the second pocket at around $z \sim 0.2, \delta \sim 0.4$ and $\alpha \sim 0.3$.

Figure 13 shows the fusion probabilities P_{CN} in the reaction ^{76}Ge+^{208}Pb for each potential energy with $E_{diss} = 0$ MeV. The blue and red lines denote P_{CN} with $V_{LD} + V_{SH}(T = 0)$ and $V_{LD} + V_{SH}(T)$, respectively. P_{CN} with V_{LD} is represented by the black line. With increasing incident energy, P_{CN} with $V_{LD} + V_{SH}(T)$ approaches that with V_{LD} owing to the disappearance of shell correction energy at high temperature.

The mass distributions of fission fragments in the reaction ^{76}Ge+^{208}Pb at $E^* = 40$ MeV are shown in Fig. 14. The blue and red lines denote the cases of $V_{LD} + V_{SH}(T = 0)$ and $V_{LD} + V_{SH}(T)$ with $E_{diss} = 0$ MeV, respectively. In the latter case, some part of the shell correction energy disappears and the number of mass symmetric fission events increases in comparison with that in the $V_{LD} + V_{SH}(T = 0)$ case.
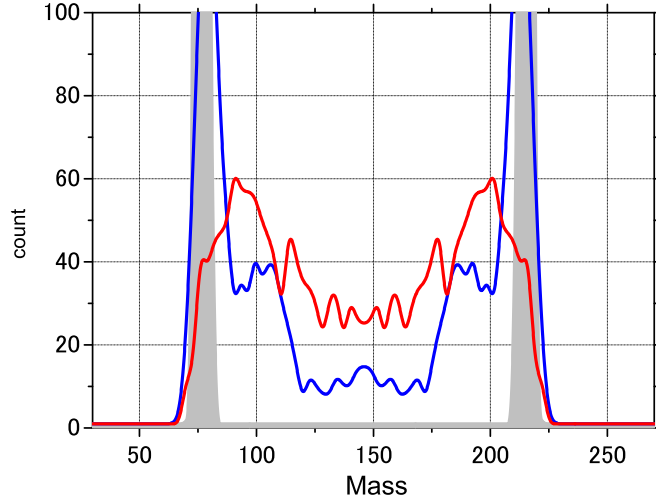
Fig. 14. Mass distribution of fission fragments in the reaction ^{76}Ge+^{208}Pb at $E^* = 40$ MeV. The blue and red lines denote the cases of $V_{LD} + V_{SH}(T = 0)$ and $V_{LD} + V_{SH}(T)$ with $E_{diss} = 0\%$, respectively. The gray shadow denotes the case of $V_{LD} + V_{SH}(T)$ with $E_{diss} = 100\%$.

4.3 E_{diss} dependence on dynamical process

Next, we focus on the dependence on E_{diss}. As discussed in references (27; 40), the fusion probability and mass distribution of fission fragments are affected by E_{diss}. When we use the condition $E_{diss} = 0$ MeV (or $E_{diss} = 0\%$), we assume that the velocity of the trajectory is in the $-z$ direction at the contact point, so that there exists trajectories that enter the fusion region. However, when we take the condition in which all the kinetic energy has already dissipated at the contact point, which is represented by $E_{diss} = 100\%$, all trajectories move down along the steep slope in the fission direction (the $+z$ direction) immediately. As a result, the fusion probability is equal to zero. We discuss this point in connection with the potential energy surface near the contact point in section 4.5.

First, we investigate the evolution of $\Phi(T)$ related to E_{diss}. When the kinetic energy dissipates during the approaching process, some part of the shell correction energy has already disappeared at the contact point. Figure 15 shows the time evolution of $\Phi(T)$ for a trajectory at $E^* = 40$ MeV with various E_{diss}. At $t = 0$ sec, $\Phi(T)$ strongly depends on E_{diss}. In this case, the potential energy surface at the contact point for each E_{diss} is shown in Fig. 16. Owing to the strong friction, 60% of the shell correction energy is rapidly lost by 7.5×10^{-22} sec. After this time, the trajectory of each E_{diss} moves on almost the same potential energy surface.
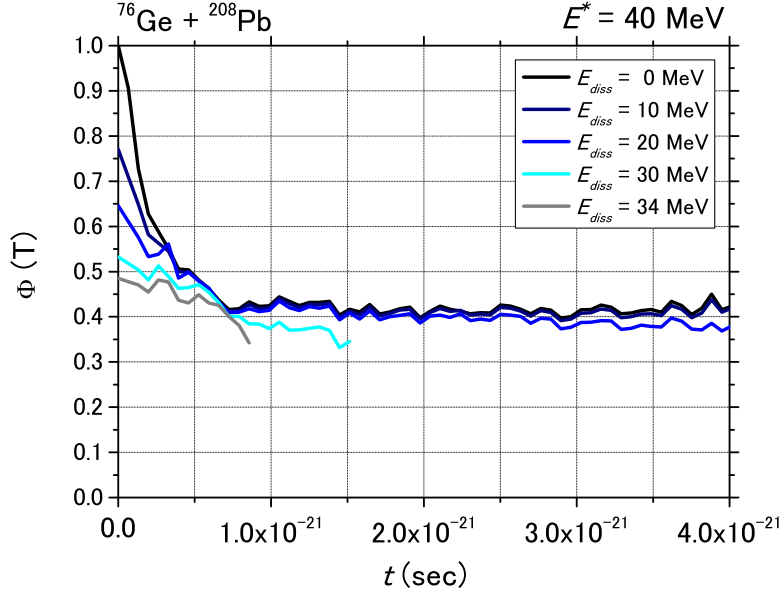
Fig. 15. Time evolution of $\Phi(T)$ for a trajectory in the reaction ^{76}Ge+^{208}Pb at $E^* = 40$ MeV for various E_{diss} cases.

In Fig. 15, the gray line denotes $\Phi(T)$ for $E_{diss} = 100\%$, which corresponds to $E_{diss} = 34$ MeV in this case. In fact, in the surface friction model, it shows that all the kinetic energy dissipates during the approaching process (41; 42). Under this condition, the gray line shows that 50% of the shell correction energy has already disappeared at the contact point. The trajectory moves down the steep slope rapidly and arrives at the fission region at 8.0×10^{-22} sec. The mass distribution of the fission fragments in this reaction is denoted by the gray shadow in Fig. 14. As discussed in reference (40), it shows the two sharp peaks corresponding to target-like and projectile-like fragments.

The fusion probabilities for the various E_{diss} cases are shown in Fig. 17. We can roughly say that the fusion probability of each E_{diss} shifts by as much as E_{diss} MeV from the black line in the $E_{diss} = 0$ MeV case. For example, in Fig. 17, we connect the points that have the same value of $E^* - E_{diss}$ at the contact point using the red dashed line. On this dashed line, the fusion probability with the large E_{diss} increases owing to the thermal fluctuation of the collective motion. However, we can see the systematic tendency and the relationship between the fusion probability and E_{diss}. Even though we treat E_{diss} as a parameter in our model, the mechanism of the dynamical process after the contact point is clarified.
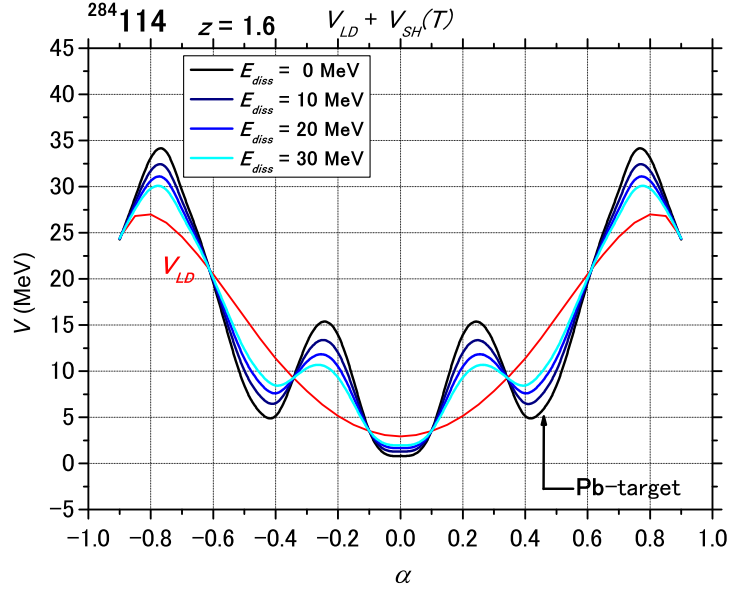
Fig. 16. Potential energy surface $V_{LD} + V_{SH}(T)$ at the contact point in the reaction ^{76}Ge+^{208}Pb at $E^* = 40$ MeV for various E_{diss} cases.

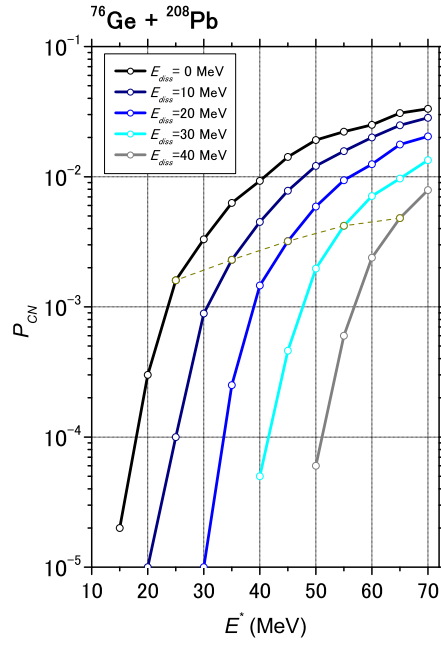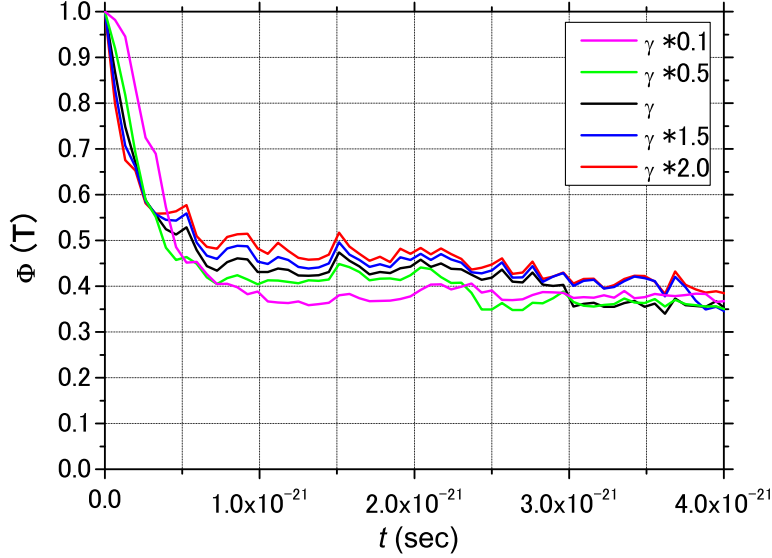Fig. 17. Fusion probabilities P_{CN} in the reaction ^{76}Ge+^{208}Pb with $V_{LD} + V_{SH}(T)$ for various E_{diss} cases.

Fig. 18. Time evolution of $\Phi(T)$ for the different friction tensors γ in the reaction ^{76}Ge+^{208}Pb at $E^* = 40$ MeV with $E_{diss} = 0$ MeV.

4.4 Friction tensor dependence on dynamical process

In the dynamical process, the dissipation speed is controlled by the friction tensor γ. That is to say, the time evolution of E_{int} depends on γ. The ambiguity of the friction tensor derived from the macroscopic model has been discussed very often (43; 44; 45). Moreover, as for the effect of nuclear structure, we should consider the microscopic transport coefficients, that are calculated by the linear response theory (16; 17; 18). The friction tensor that calculated by the microscopic model depends on the temperature and is smaller than that calculated by the macroscopic model at low temperature. Here, using the modified strength of the one-body friction tensor, we investigate the effect of the friction tensor on the dynamical process, in terms of the variational speed of the potential energy surface.

Figure 18 shows the time evolution of $\Phi(T)$ for the different friction tensors in the reaction ^{76}Ge+^{208}Pb at $E^* = 40$ MeV with $E_{diss} = 0$ MeV. The factors multiplied with the friction tensor are 0.1, 0.5, 1.0, 1.5 and 2.0, and the corresponding results are shown. Except in the case of the multiplied factor 0.1, more than 40% of the shell correction energy disappears till 3.0×10^{-22} sec for all cases. This time is rather short in comparison with the reaction time in the whole dynamical process. After $t = 5.0 \times 10^{-22}$ sec, in the smaller friction case, $\Phi(T)$ decreases faster than in the larger friction case. In the smaller friction case, after the trajectory overcomes the fusion barrier rapidly, the tra-
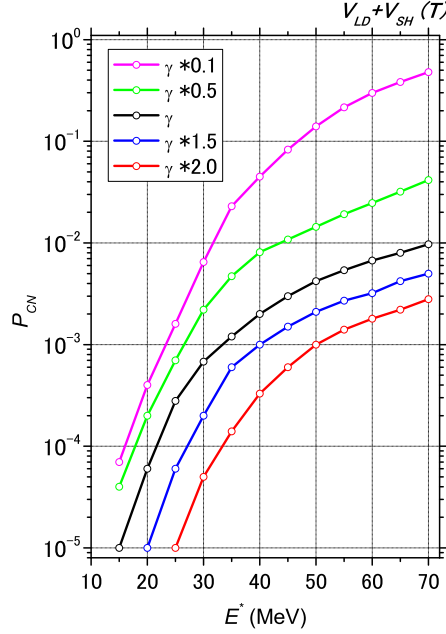
Fig. 19. Fusion probabilities P_{CN} for the different friction tensor γ in the reaction ^{76}Ge+^{208}Pb with $E_{diss} = 0$ MeV. $V_{LD} + V_{SH}(T)$ is employed.

jectory enters the region where the potential energy is lower than that near the contact point. It is possible that the variation in the potential energy is transformed into the intrinsic energy by Eq. (6). In this way, after the trajectory overcomes the fusion barrier at high speed, the intrinsic energy increases and the shell correction energy disappears rapidly. The intrinsic energy increases, not only owing to the dissipation from kinetic energy, but also owing to the transformation of the variation from the potential energy.

Figure 19 shows the fusion probabilities P_{CN} for each friction tensor for the reaction ^{76}Ge+^{208}Pb with $E_{diss} = 0$ MeV. P_{CN} increases with decreasing magnitude of the friction tensor. The friction tensor affects the dynamical process considerably (27).

We investigate the mass distribution of fission fragments for each friction tensor for the reaction ^{76}Ge+^{208}Pb at $E^* = 40$ MeV with $E_{diss} = 0$ MeV, which is shown in Fig. 20. In the small friction case, mass symmetric fission events are dominant, because the trajectory can reach the small z region. On the other hand, mass asymmetric fission events are dominant in the large friction case. The smallest value of z that the trajectory can reach is related to the mass distribution of fission fragments (15).
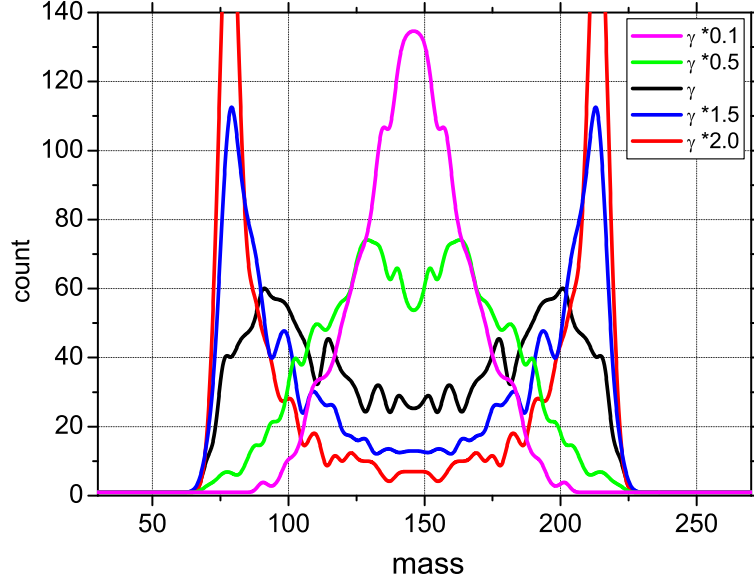
24

Fig. 20. Mass distribution of fission fragments for each friction tensor γ in the reaction ^{76}Ge+^{208}Pb at $E^* = 40$ MeV with $E_{diss} = 0$ MeV

4.5 Effect of modified potential energy surface

As we mentioned in section 4.3, when all the kinetic energy dissipates during the approaching process ($E_{diss} = 100\%$), all trajectories move down the steep slope in the fission direction and the mass distribution of fission fragments has two sharp peaks, as shown in Fig. 14. In connection with this problem, we should precisely investigate the landscape of the potential energy surface near the contact point. The modification of the potential energy near the contact point is performed continuously (46).

As a problem in our two-center shell model, since we employ the mass asymmetry parameter α, the charge distribution of the nuclei follows α. In the fusion process, this is not the proper assumption before the contact point, which we call the two-body region. At least, in the two-body region, we should calculate the potential energy using realistic distributions for the proton charge α_Z and mass α_M of the projectile and target. By performing the analysis in this manner in the two-body region, we obtain the modified potential energy surface by employing the proper smoothing between the two-body region and the one-body region at the contact point, which is denoted by the blue line in Fig. 21. It shows the ^{48}Ca+^{244}Pu reaction case, where both colliding nuclei are assumed to have a spherical shape. The red line denotes the potential energy using the same distributions of α for the charge and mass of both nuclei, even in the two-body region, that were used in the previous calculation. The open
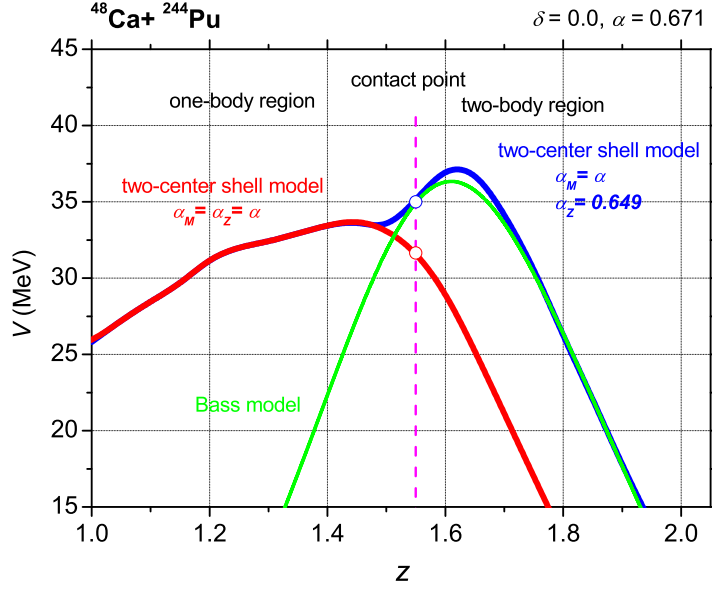
25

Fig. 21. Potential energy in the reaction ^{48}Ca+^{244}Pu calculated using the two-center shell model. The red line denotes the potential energy using $\alpha_M = \alpha_Z$ for all region. The blue line denotes the modified potential V^{mod} using α_M and α_Z of the projectile and target in the two-body region. The potential energy calculated using the Bass model is denoted by the green line. Symbols denote in the text.

circles denote the contact point of the colliding partner. The Coulomb barrier of the modified potential energy agrees with that calculated using the Bass model, which is denoted by the green line (32).

Using the modified potential energy surface, which is represented by V^{mod}, we calculate the fusion probability and mass distribution of fission fragments using the same procedure as in the previous section. We start the Langevin calculation at the contact point. We also take into account the temperature dependence of shell correction energy.

In the case of $E_{diss} = 0$ MeV, the fusion probability with the modified potential V^{mod} does not change considerably compared with the previous results. Since the velocity of the trajectory is in the $-z$ direction, it is easy to enter the small z region, and it is not affected by the potential energy surface in the two-body region. In the case of $E_{diss} = 0$ MeV, Fig. 22 shows P_{CN} using the previous potential and the modified potential, which are denoted by the red and blue lines, respectively.

On the other hand, when all the kinetic energy dissipates during the approaching process, even though the fusion probability with the previous potential is zero for any incident energy, it markedly increases in the case of the modified
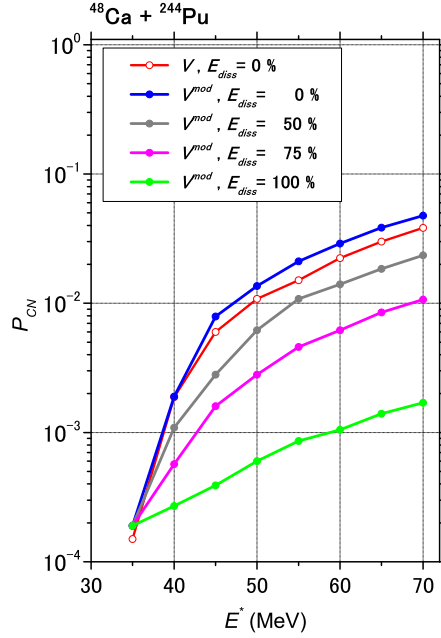
26

Fig. 22. Fusion probabilities P_{CN} in the reaction ^{48}Ca+^{244}Pu for each potential. In the case of $E_{diss} = 0$ MeV, P_{CN} using the previous potential energy V is denoted by the red line. P_{CN} using the modified potential energy V^{mod} for the different E_{diss} are denoted by each line.

potential V^{mod}, which is denoted by the green line in Fig. 22. In the V^{mod} case, the Coulomb barrier located at $z = 1.63$ prevents the trajectory from moving into the fission region immediately, and the trajectory at the contact point moves down along the potential slope in the $-z$ direction automatically. In this case, the trajectory has the momentum to go to the fusion region. In Fig. 22, we also show P_{CN} in the $E_{diss} = 50\%$ and 75 % cases with V^{mod}. P_{CN} decreases with increasing E_{diss}.

Figure 23 shows the mass distribution of fission fragments with the modified potential energy surface, in the reaction ^{48}Ca+^{244}Pu at $E^* = 36.5$ MeV. When all the kinetic energy dissipates during the approaching process, the results with the previous and modified potential energy surfaces are denoted by the red shadow and green lines, respectively. Whereas the result with the previous potential shows two sharp peaks, that with the modified potential is distributed around the wide mass region. The tendency of the latter shows a rather good agreement with the experimental data, which correspond to fusion-fission and quasi-fission events, as denoted by the black line (47). Here, the experimental data are normalized to agree with the results in the V^{mod} case with $E_{diss} = 100\%$ at the mass symmetric point. Also, we plot the results of different E_{diss} cases in Fig. 23.

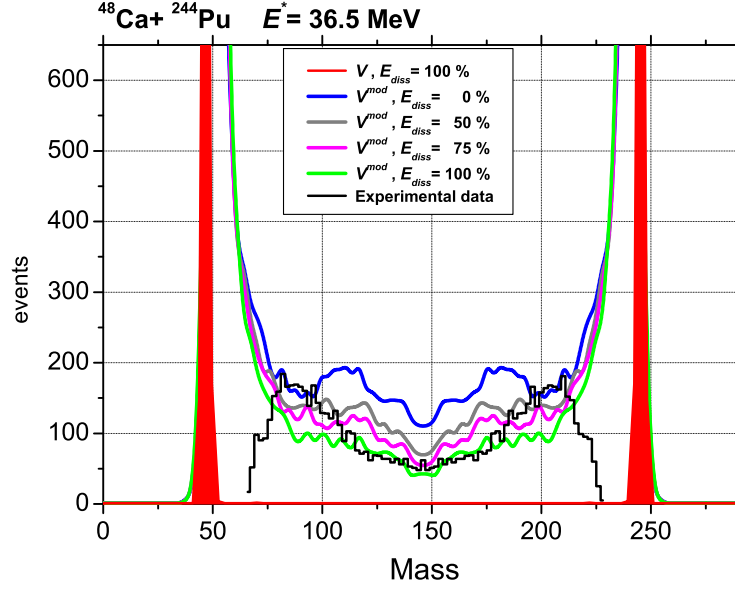Even though this result is a preliminary one, it shows the importance of the

27

Fig. 23. Mass distributions of fission fragments with the modified potential energy V^{mod} in the reaction ^{48}Ca+^{244}Pu at $E^* = 36.5$ MeV for the different E_{diss}. The red shadow denotes the mass distributions using the previous potential energy with $E_{diss} = 0$ MeV. The experimental data is denoted by black line (47).

potential energy surface near the contact point and E_{diss}. We should investigate more precisely the effect of the approaching process with the modified potential energy.

5   Summary

The dynamical process in the superheavy mass region was studied systematically by trajectory calculation in three-dimensional coordinate space. To understand the fusion mechanism clearly, we treated the dynamical process as a fusion hindrance and as a fusion enhancement, separately.

On the basis of our previous results (8), we discussed the fusion enhancement. We introduced shell correction energy on the potential energy surface, and investigated how trajectory is affected by shell correction energy.

The fusion probability increases along the cold fusion valleys at low incident energy. This is caused by the potential energy surface near the contact point on the $z - \delta$ plane. With shell correction energy, the second pocket appears at the location with a deformed shape. When the position of the second pocket corresponds to the turning point, it enhances the fusion probability.

The temperature dependence of shell correction energy was also discussed. In the dynamical process, the evolution of $\Phi(T)$ is related to E_{diss} and the friction tensor γ. We analyzed the trajectory on the temperature-dependent potential energy surface, and clarified the effects of E_{diss} and γ. The fusion probability and mass distribution of fission fragments were calculated.

This study is the first systematic attempt to investigate the role of shell correction energy in the dynamical process. Shell correction energy plays a very important role in the fusion process and enhances the fusion probability, when the colliding partner has a strong shell structure. Although we treated E_{diss} as a parameter, after the both nuclei touch, the mechanism of the dynamical process and the relationship among the parameters are clarified.

As a topic of further study, the potential energy surface should be improved near the contact point and we should investigate the dynamical process more accurately (46). We should take into account the dynamics in the approaching process and clarify how the kinetic energy dissipates in the approaching process. Also, we should directly apply the transport coefficients calculated using the microscopic model, for example, linear response theory (16; 17; 18).

References

[1] F. Hanappe, M. Lefort, C. Ngo, J. Peter, and B. Tmain, Phys. Rev. Lett. **32** (1974) 738.

[2] J. Peter, C. Ngo, F. Plasil, B. Tamain, B. Berlanger, and F. Hanappe, Nucl. Phys. A **279** (1977) 110.

[3] C. Lebrun, F. Hanappe, J. Lecolley, F. Lefebvres, C. Ngo, J. Peter, and B. Tamain, Nucl. Phys. A **321** (1979) 207.

[4] W.J. Swiatecki, Physica Scripa, **24** (1981) 113; Nucl. Phys. A **376** (1982) 275.

[5] J.P. Blocki, H. Feldmeier and W.J. Swiatecki, Nucl. Phys. A **459** (1986) 145.

[6] Y. Aritomo and M. Ohta, Nucl. Phys. A **744** (2004) 3.

[7] Swiatecki W J, Siwek-Wilczyska K and Wilczyski J 2005 *Phys. Rev.* C **71** 014602.

[8] Y. Aritomo and M. Ohta, Nucl. Phys. A **764** (2006) 149-159.

[9] S. Mitsuoka, H. Ikezoe, K. Nishio, and J. Lu, Phys. Rev. C **62** (2000) 054603.

[10] K. Nishio, H. Ikezoe, S. Mitsuoka, and J. Lu, Phys. Rev. C **62** (2000) 014602, **63** (2001) 044610.

[11] K. Satou, H. Ikezoe, S. Mitsuoka, K. Nishio, and S.C. Jeong, Phys. Rev. C **65** (2002) 054602.

[12] H. Ikezoe, K. Satou, S. Mitsuoka, K. Nishio, and S.C. Jeong, Phys. Atom. Nucl. **66** (2003) 1053.

[13] S. Hofmann and G. Munzenberg, Rev. Mod. Phys. 72 (2000) 733; S. Hofmann et al., Eur. Phys. J. A 14 (2002) 147.

[14] K. Morita et al., Nucl. Phys. A **734** (2004) 101; K. Morita et al., Journal of the Physical Society of Japan, **73** (2004) 2593.

[15] Y. Aritomo and M. Ohta, Nucl. Phys. A **753** (2005) 152; nucl-th/0502042.

[16] F.A. Ivanyuk, H. Hofmann, V.V. Pashkevich, S. Yamaji, Phys. Rev. C **55** (1997), 1730.

[17] H. Hofmann, Phys. Rev. **284** (1997), 137.

[18] S. Yamaji, F.A. Ivanyuk, H. Hofmann, Nucl. Phys. A **612** (1997), 1.

[19] R.K. Gupta and W. Greiner, *Heavy Elements and Related New Phenomena* edited by W. Greiner and P.K. Gupta (World Scientific 1999) p. 397.

[20] W. Greiner, Proc. of Fusion Dynamics at the Extremes, Dubna, 2000 (World Scientific, Singapore, 2001) p.1.

[21] J. Maruhn and W. Greiner, Z. Phys. **251** (1972) 431.

[22] K. Sato, A. Iwamoto, K. Harada, S. Yamaji, and S. Yoshida, Z. Phys. A **288** (1978) 383.

[23] J. Blocki, Y. Boneh, J.R. Nix, J. Randrup, M. Robel, A.J. Sierk and W.J. Swiatecki, Ann. Phys. **113** (1978) 330.

[24] J.R. Nix and A.J. Sierk, Nucl. Phys. A **428** (1984) 161c.

[25] H. Feldmeier, Rep. Prog. Phys. **50** (1987) 915.

[26] H.J. Krappe, J.R. Nix, and A.J. Sierk, Phys. Rev. C **20** (1979) 992.

[27] Y. Aritomo, M. Ohta, T. Materna, F. Hanappe, O. Dorvaux and L. Stuttge, Nucl. Phys. A **759** (2005) 309.

[28] S. Suekane, A. Iwamoto, S. Yamaji and K. Harada, JAERI-memo, (1974) 5918.

[29] A. Iwamoto, S. Yamaji, S. Suekane and K. Harada, Prog. Theor. Phys. **55** (1976) 115.

[30] P. Moller, J.R. Nix, P. Armbruster, S. Hofmann, G. Munzenberg, Z. Phys. A **359** (1997) 251.

[31] Yu.Ts. Oganessian et al., Nucl. Phys. A **239**, (1975) 353.

[32] R. Bass, Nucl. Phys. A **231** (1974) 45.

[33] A.N. Ignatyuk, G.N. Smirenkin, A.S. Tishin, Sov. J. Nucl. Phys. bf 21 (1975) 255.

[34] A.N. Ignatyuk, K.K. Istekov, G.N. Smirenkin, Sov. J. Nucl. Phys. **30**

(1979) 626.

[35] W. Reisdorf and M. Schodel, Z. Phys. A **343** (1992) 47.

[36] M. Diebel, K. Albrecht, R.W. Hasse, Nucl. Phys. A **355** (1981) 66.

[37] Z. Lojewski, V.V. Pashkevich, S. Cwiok, Nucl. Phys. A **436** (1985) 499.

[38] Y. Aritomo, T. Wada, M. Ohta, and Y. Abe, Phys. Rev. C **59** (1999) 796.

[39] J. Toke and W.J. Swiatecki, Nucl. Phys. A **372** (1981) 141.

[40] Y. Aritomo and M. Ohta, Yderna Fiz. **66** (2003) 1141.

[41] D.H.E. Gross and H. Kalinowski, Phys. Rept. 45 (1978) 175.

[42] P. Froebrich et. al, Nucl. Phys. A **406** (1983) 557.

[43] T. Wada, N. Carjan and Y. Abe, Nucl. Phys. A **538** (1992) 283c.

[44] D. Hilscher and H. Rossner, Proceedings of the International School-Seminar on Heavy Ion Physcis (1993), Dubna, Russia, p230.

[45] A.V. Karpov, P.N. Nadtochy, D.V. Vanin, and G.D. Adeev, Phys. Rev. C **63** (2001) 054610.

[46] V.I. Zagrebaev, A.V. Karpov, M.A. Naumenko and W. Greiner, private communication.

[47] M.G. Itkis et al., Proceeding of Fusion Dynamics at the Extremes (World Scientific, Singapore, 2001) p93.